Monthly Notices of the ROYAL ASTRONOMICAL SOCIETY

MNRAS **461,** 2944–2952 (2016) doi:10.1093/mnras/stw1509
Advance Access publication 2016 June 26

ALMA observations of a $z \approx 3.1$ protocluster: star formation from active galactic nuclei and Lyman-alpha blobs in an overdense environment

D. M. Alexander,[1⋆] J. M. Simpson,[1] C. M. Harrison,[1] J. R. Mullaney,[2] I. Smail,[1] J. E. Geach,[3] R. C. Hickox,[4] N. K. Hine,[3] A. Karim,[5] M. Kubo,[6,7] B. D. Lehmer,[8] Y. Matsuda,[9,10] D. J. Rosario,[1] F. Stanley,[1] A. M. Swinbank,[1] H. Umehata[11,12] and T. Yamada[13]

[1]*Centre for Extragalactic Astronomy, Department of Physics, Durham University, South Road, Durham DH1 3LE, UK*
[2]*Department of Physics and Astronomy, The University of Sheffield, Hounsfield Road, Sheffield S3 7RH, UK*
[3]*Centre for Astrophysics Research, Science and Technology Research Institute, University of Hertfordshire, Hatfield AL10 9AB, UK*
[4]*Department of Physics and Astronomy, Dartmouth College, 6127 Wilder Laboratory, Hanover, NH 03755, USA*
[5]*Argelander-Institut für Astronomie, Universität Bonn, Auf dem Hügel 71, D-53121 Bonn, Germany*
[6]*Institute for Cosmic Ray Research, University of Tokyo, 5-1-5 Kashiwa-no-Ha, Kashiwa City, Chiba 277-8582, Japan*
[7]*Astronomical Institute, Tohoku University, 6-3 Aoba, Aramaki, Aoba-ku, Sendai, Miyagi 980-8578, Japan*
[8]*University of Arkansas, 226 Physics Building, Fayetteville, AR 72701, USA*
[9]*National Astronomical Observatory of Japan, 2-21-1 Osawa, Mitaka, Tokyo 181-8588, Japan*
[10]*Graduate University for Advanced Studies (SOKENDAI), Osawa 2-21-1, Mitaka, Tokyo 181-0015, Japan*
[11]*European Southern Observatory, Karl-Schwarzschild-Str. 2, D-85748 Garching, Germany*
[12]*Institute of Astronomy, School of Science, The University of Tokyo, 2-21-1 Osawa, Mitaka, Tokyo 181-0015, Japan*
[13]*Astronomical Institute, Tohoku University, 6-3 Aoba, Aramaki, Aoba-ku, Sendai, Miyagi 980-8578, Japan*

Accepted 2016 June 21. Received 2016 June 21; in original form 2015 December 23

ABSTRACT

We exploit Atacama Large Interferometer Array (ALMA) 870 μm observations to measure the star formation rates (SFRs) of eight X-ray detected active galactic nuclei (AGNs) in a $z \approx 3.1$ protocluster, four of which reside in extended Lyα haloes (often termed Lyman-alpha blobs: LABs). Three of the AGNs are detected by ALMA and have implied SFRs of $\approx$220–410 $M_\odot$ yr^{-1}; the non-detection of the other five AGNs places SFR upper limits of $\lesssim$210 $M_\odot$ yr^{-1}. The mean SFR of the protocluster AGNs ($\approx$110–210 $M_\odot$ yr^{-1}) is consistent (within a factor of $\approx$0.7–2.3) with that found for co-eval AGNs in the field, implying that the galaxy growth is not significantly accelerated in these systems. However, when also considering ALMA data from the literature, we find evidence for elevated mean SFRs (up-to a factor of $\approx$5.9 over the field) for AGNs at the protocluster core, indicating that galaxy growth is significantly accelerated in the central regions of the protocluster. We also show that all of the four protocluster LABs are associated with an ALMA counterpart within the extent of their Lyα emission. The SFRs of the ALMA sources within the LABs ($\approx$150–410 $M_\odot$ yr^{-1}) are consistent with those expected for co-eval massive star-forming galaxies in the field. Furthermore, the two giant LABs (with physical extents of $\gtrsim$100 kpc) do not host more luminous star formation than the smaller LABs, despite being an order of magnitude brighter in Lyα emission. We use these results to discuss star formation as the power source of LABs.

Key words: galaxies: active – galaxies: evolution – quasars: general – galaxies: star formation – submillimetre: galaxies.

1 INTRODUCTION

A key goal of observational cosmology is to understand how galaxies and massive black holes (BHs) grow as a function of environment. Models of large-scale structure formation predict that galaxy and BH growth in distant high-density regions will be accelerated in comparison to the growth of systems in typical regions of the distant Universe (i.e. the field; e.g. Kauffmann, Nusser & Steinmetz 1997; Governato et al. 1998; de Lucia et al. 2006; Benson 2010; Alexander & Hickox 2012). These distant high-density regions can be identified as protoclusters (e.g.

⋆ E-mail: d.m.alexander@durham.ac.uk

Governato et al. 1998; Chiang, Overzier & Gebhardt 2013), structures where gravitational collapse and coalescence has not yet been sufficient to produce a virialized galaxy cluster. Direct comparisons between the observed growth rates of galaxies and BHs in protoclusters to systems in the field can reveal whether galaxy and BH growth is accelerated in distant high-density regions of the Universe.

One of the best studied high-density regions in the distant Universe is the $z \approx 3.09$ protocluster in the SSA 22 field. The SSA 22 protocluster was originally identified as a significant overdensity (factor ≈4–6 when compared to the field) of Lyman-Break Galaxies and is predicted to evolve into a $\approx 10^{15}$ $M_{\odot}$ galaxy cluster (i.e. similar to the Coma cluster) by the present day (e.g. Steidel et al. 1998, 2000; Kubo et al. 2015). The protocluster has been traced over a 60 × 10 Mpc^2 (comoving) region using narrow-band imaging at rest-frame Lyα wavelengths, which also reveals a significant overdensity of Lyα Emitters (LAEs; e.g. Hayashino et al. 2004; Matsuda et al. 2005; Yamada et al. 2012a) and regions of extended ($\gtrsim$30 kpc) Lyα emission (often termed Lyman-alpha blobs, LABs; e.g. Steidel et al. 2000; Matsuda et al. 2004; Yamada et al. 2012a) when compared to the field. The SSA 22 protocluster therefore provides an ideal environment to test whether galaxy and BH growth is accelerated in a distant high-density environment.

Deep *Chandra* observations of the SSA 22 protocluster have revealed a significant enhancement (factor $6.1^{+10.3}_{-3.6}$) in the fraction of galaxies that host active galactic nucleus (AGN) activity above a given X-ray luminosity threshold when compared to the field at $z \approx 3$ (Lehmer et al. 2009b). The increase in the AGN fraction indicates an increase in the duty cycle of AGN activity (i.e. the duration of significant BH growth rates) over that found in the field. Given the broad connection between AGN activity and star formation and the various tight relationships between BH mass and the properties of nearby galaxies (e.g. Alexander & Hickox 2012; Graham & Scott 2013; Kormendy & Ho 2013), we may also expect an enhancement in the amount of star formation per galaxy in the SSA 22 protocluster. This hypothesis can be tested by measuring the star formation rates (SFRs) of the AGNs and galaxies in the protocluster. However, with the exception of the deep ALMA observations of the protocluster core by Umehata et al. (2015), the existing SFR measurements for the SSA 22 protocluster have been taken at wavelengths where the emission is either easily obscured by dust (e.g. the ultraviolet continuum or Lyα emission; Matsuda et al. 2005) or the data is too shallow to provide sensitive individual SFR constraints on all but the brightest sources (single-dish far-infrared–millimetre observations; e.g. Geach et al. 2005, 2014; Scott, Dunlop & Serjeant 2006; Tamura et al. 2009, 2010, 2013; Umehata et al. 2014).

In this paper, we present ALMA 870 μm observations of eight X-ray detected AGNs in the SSA 22 protocluster to provide sensitive SFR measurements from even the most heavily obscured star-forming regions in these sources. The main objective of this paper is to provide sensitive constraints on the SFRs of AGNs in a distant protocluster environment and to assess whether the host galaxies are growing more rapidly than co-eval AGNs in the field. Four of the eight X-ray AGNs are also coincident with LABs and we use our data to provide insight on the star formation properties of LABs. We have adopted $H_0 = 71\,km\,s^{-1}$, $\Omega_M = 0.27$ and $\Omega_\Lambda = 0.73$; in this cosmology 1 arcsec corresponds to 7.8 kpc at $z = 3.09$. In our SFR calculations, we have assumed the Chabrier (2003) initial mass function.

2 DATA

2.1 Sample selection

We selected our eight ALMA targets from the *Chandra* catalogues of Lehmer et al. (2009a,b) in the SSA 22 field. All of the targets have spectroscopic redshifts of $z = 3.08$–3.11, placing them well within the redshift range of the SSA 22 protocluster (Matsuda et al. 2005). All of the targets are also luminous at X-ray energies, with X-ray luminosities of $L_{2-32\,keV} = (0.9\text{–}4.2) \times 10^{44}$ erg s^{-1}, indicating that they are X-ray AGNs.[1] The high rest-frame energies probed by the *Chandra* data at $z \approx 3.09$ (2–32 keV) also mean that all but the most heavily obscured luminous AGNs (i.e. $N_H \lesssim 10^{24}$ cm^{-2}) will be detected and identified in the X-ray band (e.g. Alexander et al. 2008; Brandt & Alexander 2015; Del Moro et al. 2016). We have not attempted to correct the X-ray luminosities for obscuration since the corrections will only be significant for the most heavily obscured systems and would require detailed X-ray spectral analyses and higher quality X-ray data than currently available to measure accurate column densities.[2]

Our sample includes all six of the X-ray AGNs identified at $z \approx 3.09$ in Lehmer et al. (2009b) plus two additional X-ray AGNs from Lehmer et al. (2009a) that have been spectroscopically identified as lying at $z \approx 3.09$ (AGN 7: $z = 3.098$; Saez et al. 2015; AGN 8: $z = 3.091$; Kubo et al. 2015). This sample also contains four of the five X-ray-detected LABs in Geach et al. (2009). However, there are several X-ray AGNs in the protocluster that we did not observe with ALMA (Tamura et al. 2010; Kubo et al. 2013; Umehata et al. 2015), including LAB 18 from Geach et al. (2009). On the basis of optical spectral analyses (Steidel et al. 2003; Yamada et al. 2012b; Kubo et al. 2015), five of the X-ray AGNs in our sample have narrow emission lines and therefore appear to be optically obscured AGNs while three have broad emission lines and are therefore optically unobscured AGNs. Four of the X-ray AGNs are identified as LABs (LAB 2; LAB 3; LAB 12; LAB 14), two of which have physical extents of $\gtrsim$100 kpc and are defined as giant LABs (LAB 2; LAB 3; Matsuda et al. 2011).

All of our targets are detected in the narrow-band rest-frame Lyα imaging of Matsuda et al. (2004). In Fig. 1, we plot the Lyα luminosity versus the X-ray luminosity of the ALMA targets. The mean X-ray and Lyα luminosities of the LABs and non-LABs are comparable: $\log(L_{2-32\,keV}/erg\ s^{-1}) = 44.1 \pm 0.2$ and $\log(L_{Ly\alpha}/erg\ s^{-1}) = 43.4 \pm 0.5$ for the LABs and $\log(L_{2-32\,keV}/erg\ s^{-1}) = 44.1 \pm 0.2$ and $\log(L_{Ly\alpha}/erg\ s^{-1}) = 43.3 \pm 0.3$ for the non-LABs. However, overall the ALMA targets cover a broad range in Lyα/X-ray luminosity ratio. The Lyα/X-ray luminosity ratio provides insight on the AGN contribution to the Lyα emission, which is discussed in Section 3.2. We note that the distinction between LABs and non-LABs is not based on Lyα luminosity but is a function of both the extent and surface brightness of the Lyα emission; see section 3 of Matsuda et al. (2004). The mean Lyα luminosity of the X-ray-undetected LABs in the SSA 22 protocluster ($\log(L_{Ly\alpha}/erg\ s^{-1}) = 43.1 \pm 0.3$) is also similar to the

[1] We note that the rest-frame 2–32 keV luminosity is a factor of 2.2 larger than the more commonly used rest-frame 2–8 keV luminosity, assuming a typical X-ray spectral slope of $\Gamma = 1.9$.

[2] For example, corrections to the rest-frame 2–32 keV luminosity due to obscuration are only a factor $\gtrsim$2 when $N_H \gtrsim 8 \times 10^{23}$ cm^{-2} for a typical X-ray spectral slope of $\Gamma = 1.9$.

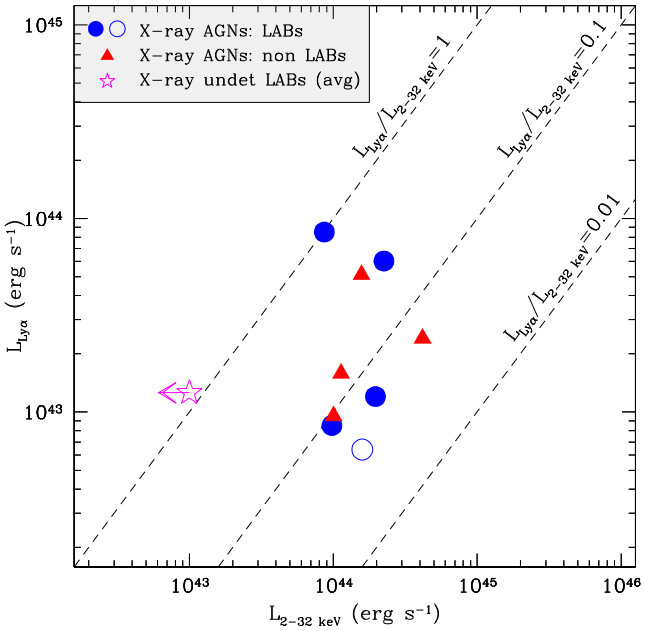

Figure 1. Lyα luminosity versus rest-frame 2–32 keV luminosity of the eight ALMA targets (filled circle: LABs; filled triangle: non-LABs), and LAB 18 (open circle). As a comparison, the average properties of the X-ray undetected LABs in the protocluster are also shown (open star). The dashed lines indicate constant ratios of Lyα and X-ray luminosity. All of the X-ray AGNs are luminous ($L_X \gtrsim 10^{44}$ erg s^{-1}) and, overall, they cover a broad range in Lyα/X-ray luminosity ratio.

ALMA targets despite being at least an order of magnitude fainter at X-ray energies ($L_{2-32\,keV} \lesssim 10^{43}$ erg s^{-1}; Geach et al. 2009).

2.2 ALMA observations and data reduction

The eight targets were observed with ALMA on 2012 November 20, as part of the Cycle 0 project 2011.0.00725. Each target was observed using a 7.5 GHz bandwidth, centred on 344 GHz (i.e. 870 μm: band 7). A single-continuum correlator set-up was used, with four basebands of 128 dual-polarization channels each. The array configuration was such that a total of 25 antennas were used, with a maximum baseline of 375 m and a median baseline of 145 m. The minimum baseline of the array is 15 m, which translates to a maximum recoverable size of ≈7 arcsec.

Each target was observed for a total of 310 s. Neptune was used as the primary flux calibrator, with J 2225−049 used for band pass and phase calibration. Neptune is known to have a CO absorption feature at 345 GHz. To minimize the impact of this feature on our flux measurements, we have modelled the data using the 2012-Butler-JPL-Horizons model for Neptune, which includes CO absorption lines. Furthermore, our ALMA observations only have coverage at 337–340 GHz and 350–353 GHz and, therefore, the CO absorption feature will have a negligible impact on our measurements.

The data were processed with the Common Astronomy Software Application (CASA v4.4.0; McMullin et al. 2007), and maps were produced using the 'clean' routine within CASA. As is the standard approach for interferometry data, we 'cleaned' each target map to reduce the strength of the side lobes from detected sources. This is required to accurately measure the properties of all detected sources and to search for faint sources that lie close to the side lobes of a bright source. For each target, we adopt an iterative approach to the clean procedure, following the method outlined in Hodge et al. (2013) and Simpson et al. (2015). We first create a 'dirty' map of each target, using natural weighting, and measure the root mean square (rms; σ) noise in the resulting map. Tight clean boxes were then placed around all sources detected at $>5\sigma$ and the dirty map is cleaned to a depth of 1.5σ within these clean boxes. We then measure the rms in this initial cleaned map, or use the rms in the dirty map if no sources are detected at $>5\sigma$, and repeat the clean procedure on all sources detected at $>3.5\sigma$ in these maps to produce a final map that is suitable for the detection of even faint sources. If no sources are detected at $>3.5\sigma$ then the dirty map is considered as the final map.

The final ALMA maps for our eight targets have a range of rms values (σ = 0.21–0.34 mJy beam^{-1}) and a median synthesized beam of 1.10 arcsec × 0.61 arcsec. We note that the synthesized beam becomes increasingly elongated at low target elevations, and the final maps have a range of beam major and minor axes of 0.99–1.45 arcsec and 0.68–0.59 arcsec, respectively; see Fig. 2 for the size and shape of the synthesized beam for each map. Each map was created with a total size of 25.6 arcsec × 25.6 arcsec and a pixel scale of 0.1 arcsec.

2.3 ALMA source detection, matching, and properties

The ALMA maps for the eight targets are shown in Fig. 2, with contours of the Lyα emission overlaid. Several apparently significant peaks at 870 μm are seen in the maps but we need to set a detection threshold to reliably distinguish between real and spurious sources. To achieve this, we initially identified all $>3.5\sigma$ peaks in the non-primary-beam-corrected ALMA maps as potential sources and then inverted the maps and repeated this detection procedure. To measure the spurious detection rate for a given significance threshold, we then simply compare the number of detected sources between the original and inverted maps as a function of the detection threshold. We find that the number of 'negative' sources falls to zero at $>4.5\sigma$, and hence to ensure that we only include robust ALMA detections we only consider peaks in the ALMA maps at $>4.5\sigma$. Overall we detect six ALMA sources at $>4.5\sigma$ within the primary beam of the ALMA maps; see Fig. 2. We measured the peak flux density and fitted a point source model at the position of each source to search for evidence of extended 870 μm emission. We do not see significant residuals after subtracting the best-fitting point source model, indicating that the sources are not resolved in our maps and corresponding to physical scales for the star formation emission of $\lesssim$11 kpc. The peak flux density in the map is therefore taken to be the flux density of each source, which we correct for the primary beam attenuation.

We searched for matches between the X-ray AGNs and the ALMA sources using the *Chandra* and ALMA positional uncertainties. For the uncertainty in the X-ray source position, we used 1.5 times the 80 per cent confidence level of each X-ray source from Lehmer et al. (2009a) and for the uncertainty in the ALMA source position we conservatively assumed 0.4 arcsec, the average ALMA positional uncertainty measured by Hodge et al. (2013). Combining these two positional uncertainties, we find that three of the six ALMA sources are directly matched with an X-ray AGN (AGN 1; AGN 5; AGN 8; see Table 1), with *Chandra*–ALMA positional offsets of 0.3–0.9 arcsec. The other three ALMA sources have 1.6–4.5 arcsec offsets from *Chandra* sources and are not directly matched to an X-ray AGN (see Table 2). The 1.6 arcsec offset (≈12 kpc in projection) between the X-ray AGN and ALMA source in AGN 7 is larger than our search radius but still close enough that

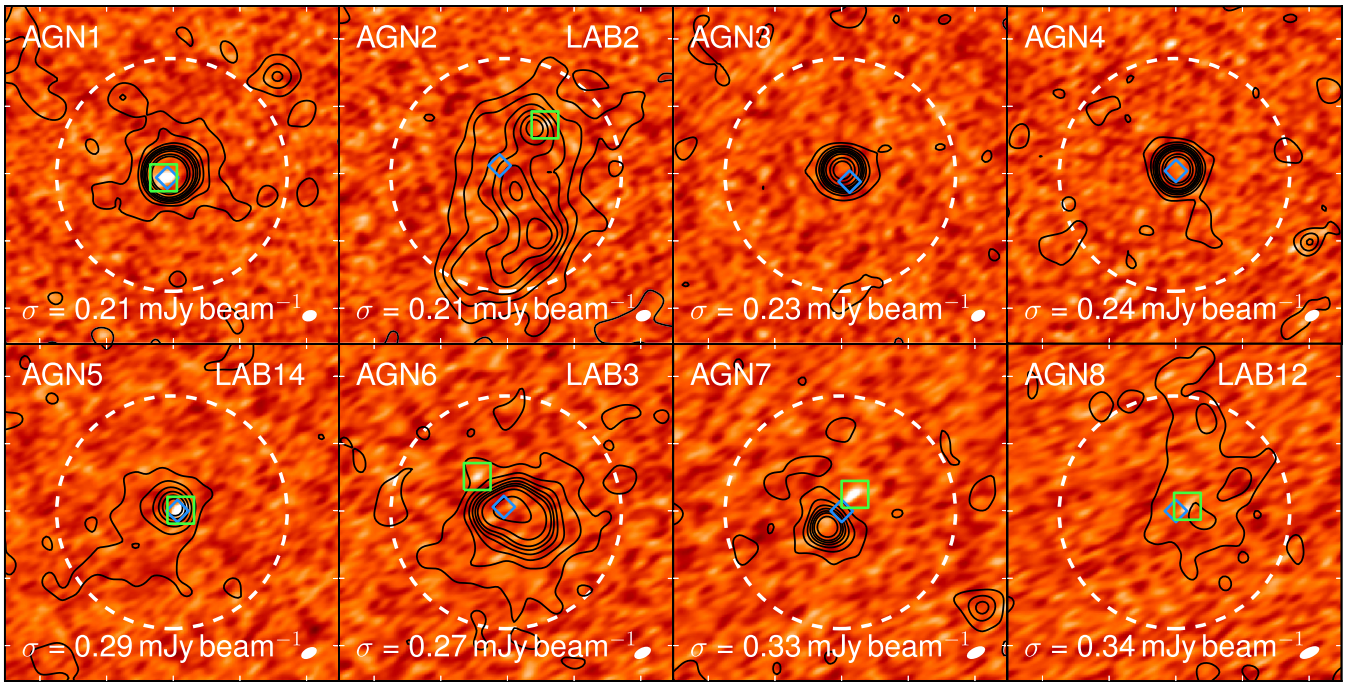

Figure 2. ALMA 870 μm maps of the eight X-ray-detected AGNs. The black contours trace the surface brightness of the Lyα emission, the blue diamond indicates the position of the X-ray AGN, the green square indicates the position of the ALMA-detected source, and the dashed circle indicates the size of the primary beam ($r = 8.7$ arcsec), which corresponds to a projected radius of 68 kpc at $z = 3.09$. The size and shape of the synthesized beam is shown in the bottom right-hand corner of each map. We find an ALMA counterpart directly matched to an X-ray AGN in three sources (AGN 1; AGN 5; AGN 8) and an ALMA counterpart offset by 1.6–4.5 arcsec from an X-ray AGN in a further three sources (AGN 2; AGN 6; AGN 7). An ALMA counterpart lies within the extent of the Lyα emission for all of the four LABs. See Tables 1 and 2 for the source properties.

the two sources may be physically associated. Indeed, investigation of publicly available optical–near-IR *Hubble Space Telescope* (*HST*) imaging shows that the X-ray AGN is matched to a point source while the ALMA source is matched to a galaxy with a disturbed morphology, suggesting that these are two distinct sources (an X-ray AGN and a galaxy) in a merger with a projected separation of ≈12 kpc. We note that a larger fraction of galaxies appear to reside in mergers in the SSA 22 protocluster when compared to co-eval galaxies in the field (Hine et al. 2016a).

The two ALMA sources in the fields of AGN 2 and AGN 6 have large *Chandra*–ALMA offsets of 2.8–4.5 arcsec (≈22–35 kpc in projection) and are not directly matched to an X-ray AGN. However, each ALMA source resides within the extended Lyα emission of a LAB (LAB 2; LAB 3). This suggests that the ALMA sources may be physically associated with the LAB; see Fig. 2. We can provide a basic test of this scenario by assessing whether we would expect to detect any sources by chance in our ALMA maps. To determine the number of sources expected in our maps by chance, we took the best-fitting model of the 870 μm number counts from Simpson et al. (2015) and calculated the number of ALMA sources that we would expect in each map, taking into account both the sensitivity of each map and the decrease in sensitivity from the phase centre. On the

Table 1. The coordinates correspond to the *Chandra* source position and the ALMA source position and the offset refers to the angular separation between the *Chandra* and ALMA source. The redshifts are all spectroscopic and are taken from Steidel et al. (2003), Matsuda et al. (2005), Kubo et al. (2015), and Saez et al. (2015). The X-ray luminosity is calculated at rest-frame 2–32 keV using the 0.5–8 keV flux from Lehmer et al. (2009a) and the Lyα luminosity is calculated using the Lyα flux from Matsuda et al. (2004); see footnote 1 for the X-ray luminosity convection to rest-frame 2–8 keV. The ALMA 870 μm measurements (source flux and uncertainty) are primary-beam-corrected values and the upper limits refer to 4.5 times the primary-bream-corrected rms. The infrared luminosity ($L_{\rm IR}$) refers to the star formation emission at rest-frame 8–1000 μm and has an uncertainty of ≈0.3 dex; see Section 2.4 for the calculation of $L_{\rm IR}$.

	ALMA properties of the X-ray-detected AGNs									
Name	$\alpha_{\rm Chandra}$ (J2000)	$\delta_{\rm Chandra}$ (J2000)	z	$L_{2-32\,\rm keV}$ (log(erg s^{-1}))	$L_{{\rm Ly}\alpha}$ (log(erg s^{-1}))	$\alpha_{\rm ALMA}$ (J2000)	$\delta_{\rm ALMA}$ (J2000)	Offset (arcsec)	$S_{870\,\mu\rm m}$ (mJy)	$L_{\rm IR}$ (log(erg s^{-1}))
AGN 1	22 17 36.54	+00 16 22.6	3.084	44.20	43.71	22 17 36.56	+00 16 22.6	0.27	1.84 ± 0.21	45.98
AGN 2 (LAB 2)	22 17 39.08	+00 13 30.7	3.091	43.94	43.93	–	–	–	<0.92	<45.68
AGN 3	22 17 09.60	+00 18 00.1	3.106	44.05	43.20	–	–	–	<1.04	<45.73
AGN 4	22 17 20.24	+00 20 19.3	3.105	44.62	43.38	–	–	–	<1.10	<45.76
AGN 5 (LAB 14)	22 17 35.84	+00 15 59.1	3.094	44.29	43.08	22 17 35.82	+00 15 59.2	0.25	2.96 ± 0.29	46.19
AGN 6 (LAB 3)	22 17 59.23	+00 15 29.7	3.096	44.35	43.78	–	–	–	<1.21	<45.80
AGN 7	22 17 16.16	+00 17 45.8	3.098	44.00	42.98	–	–	–	<1.50	<45.89
AGN 8 (LAB 12)	22 17 32.00	+00 16 55.6	3.091	43.99	42.93	22 17 31.94	+00 16 55.9	0.91	1.58 ± 0.35	45.92

Table 2. The coordinates correspond to the ALMA source position and the offset refers to the angular separation between the ALMA and *Chandra* source; see Table 1 for the *Chandra* source positions. The ALMA 870 μm measurements (source flux and uncertainty) are primary-beam corrected values. The infrared luminosity ($L_{\rm IR}$) refers to the star formation emission over rest-frame 8–1000 μm, calculated assuming $z = 3.09$, and has an uncertainty of ≈0.3 dex; see Section 2.4 for the calculation of $L_{\rm IR}$.

Name	Additional ALMA-detected sources in the protocluster				
	$\alpha_{\rm ALMA}$ (J2000)	$\delta_{\rm ALMA}$ (J2000)	Offset (arcsec)	$S_{870\mu{\rm m}}$ (mJy)	$L_{\rm IR}$ (log(erg s^{-1}))
AGN 2 (LAB 2)	22 17 38.85	+00 13 33.7	4.54	1.11 ± 0.25	45.76
AGN 6 (LAB 3)	22 17 59.34	+00 15 32.0	2.81	1.38 ± 0.29	45.86
AGN 7	22 17 16.09	+00 17 47.0	1.57	2.25 ± 0.34	46.07

basis of this simple test, overall, we predict 0.17 ALMA sources by chance within the primary beam across all of our eight ALMA maps and 0.04 ALMA sources within the primary beam across the two ALMA maps of LAB 2 and LAB 3, suggesting that the offset ALMA sources are likely to be physically associated with the LAB.

The 870 μm flux densities of the six ALMA-detected sources are 1.10–2.96 mJy. We calculated ALMA upper limits for the five X-ray AGNs without an ALMA counterpart by taking 4.5 times the rms, adjusting for any small primary beam corrections when the X-ray source does not lie at the phase centre. The ALMA properties of the eight X-ray AGNs are given in Table 1 and the ALMA properties for the three additional ALMA sources not directly matched to an X-ray AGN are given in Table 2. The only source in our sample reliably detected at submillimetre wavelengths in previous studies is the brightest ALMA source (AGN 5), which has a flux density from Submillimetre Common-User Bolometer Array observations consistent within ≈1.5σ of the ALMA flux density ($S_{850\,\mu{\rm m}} = 4.9 \pm 1.3$ mJy; Geach et al. 2005). Two of the other X-ray AGNs have been previously detected by ALMA at 1.1 mm wavelengths (AGN 1; AGN 8; Umehata et al. 2015) and our 870 μm flux densities for these two sources are ≈1.8–2.3 times higher than the 1.1 mm flux densities measured by Umehata et al. (2015), which is within the range expected for dust emission from a typical star-forming galaxy at this redshift. The flux densities of the other three ALMA-detected sources are below the sensitivity limits of previous-generation submillimetre and millimetre observatories.

2.4 Measurement of star formation rates

The rest-frame wavelengths of the ALMA data correspond to ≈210 μm at $z = 3.09$. Such long-wavelength far-infrared emission is likely to be dominated by star formation activity, which typically peaks at ≈100 μm (e.g. Brandl et al. 2006; Mullaney et al. 2011; Béthermin et al. 2015). By comparison, dust emission from AGN activity peaks at <40 μm and drops off sharply at longer wavelengths (e.g. Richards et al. 2006; Netzer et al. 2007; Mullaney et al. 2011).

We calculated the infrared luminosities ($L_{\rm IR}$ over rest-frame 8–1000 μm) from star formation using the ALMA 870 μm flux densities following section 3 of Mullaney et al. (2015). We adopted this specific approach since the Mullaney et al. (2015) study provided SFR measurements of X-ray AGNs in the field on the basis of ALMA 870 μm data, which are used as our field AGN comparison sample in Section 3. Briefly, the infrared luminosities are calculated from the 870 μm flux densities over rest-frame 8–1000 μm using the source redshifts and the average spectral energy distributions (SEDs) of the star-forming galaxies in Bethermin et al. (2015). The uncertainty on $L_{\rm IR}$ is relatively modest because the ALMA data probes close to the peak of the SED for star-forming galaxies at $z \approx 3$ and is estimated by Mullaney et al. (2015) to be ≈0.3 dex on the basis of the range of SED templates of Draine & Li (2007); see section 3 of Mullaney et al. (2015). See Tables 1 and 2 for the calculated $L_{\rm IR}$ values. SFRs are estimated from $L_{\rm IR}$ following Kennicutt (1998) for the Chabrier (2003) initial mass function; the conversion from $L_{\rm IR}$ to SFR adopted in our study is

$$\mathrm{SFR} = \frac{L_{\rm IR}}{3.778 \times 10^{43}\ \mathrm{erg\ s^{-1}}} \mathrm{M_\odot\ yr^{-1}}. \quad (1)$$

The rest-frame 210 μm emission is likely to be dominated by star formation for all but the most luminous AGNs. We can verify this and quantify the potential contribution to the ALMA flux densities from AGN activity by taking the *Spitzer* 24 μm constraints of our sources and predicting the 870 μm flux density. All of our X-ray AGNs and ALMA sources have a 24 μm flux density of $S_{24\,\mu{\rm m}} <$ 100 μJy, with the exception of AGN 1 which has $S_{24\,\mu{\rm m}} = 450 \pm$ 10 μJy (e.g. Webb et al. 2009; Colbert et al. 2011; Capak et al. 2013). On the basis of the mean empirical AGN SED template of Mullaney et al. (2011), a 24 μm flux density of 100 μJy would correspond to a 870 μm flux density of only 35 μJy at $z = 3.09$. Conservatively assuming that the 24 μm emission is dominated by AGN activity rather than star formation, we therefore predict that the AGN contributes to ≈9 per cent of the 870 μm flux density for AGN 1 and contributes to $\lesssim$4 per cent for all of the other sources. We therefore expect our 870 μm flux densities to provide a reliable measurement of the star formation luminosities of our sources.

3 RESULTS

Overall we detected six sources at 870 μm within the primary beam of the eight ALMA maps: three of the eight X-ray AGNs have ALMA counterparts, all of the four LABs have an ALMA counterpart within the extent of the Lyα emission (two of which are directly matched with an X-ray AGN and two of which are offset from the X-ray AGN but are likely to be physically associated with the LAB), and one ALMA source appears to be a galaxy in a merger with an X-ray AGN. In the following subsections, we compare the SFRs of the X-ray AGNs in the protocluster to the SFRs of distant X-ray AGNs in the field (see Section 3.1) and investigate the SFRs of the protocluster LABs (see Section 3.2).

3.1 The star formation properties of X-ray-detected AGNs in a distant protocluster

Many previous studies have explored the SFRs of distant X-ray AGNs in the field (e.g. Shao et al. 2010; Harrison et al. 2012; Mullaney et al. 2012; Rosario et al. 2012, 2013; Santini et al. 2012; Stanley et al. 2015). However, little is known about the SFRs of X-ray AGNs in a distant protocluster environment. The previous studies of field AGNs have found that both the mean SFR and

the evolution in SFR with redshift are consistent with those of co-eval massive ($\approx M_*$) star-forming galaxies (e.g. Mullaney et al. 2012; Santini et al. 2012; Hickox et al. 2014; Stanley et al. 2015); for example, the mean SFRs of X-ray AGNs at $z \approx 2.0$–2.5 are $\approx$10 times higher than those of X-ray AGNs at $z \approx 0.5$–1.0. On average, distant X-ray AGNs therefore appear to reside in typical star-forming galaxies, although we caution that there can be a broad spread of individual SFR values (e.g. Mullaney et al. 2015).

In our analyses, we compare the SFRs of X-ray AGNs in the protocluster and field, utilizing the study of Mullaney et al. (2015), which primarily used ALMA 870 μm data to measure SFRs for $z > 1.5$ X-ray AGNs in the field. The field AGNs extend to lower X-ray luminosities than the protocluster AGNs, as expected due to the deeper *Chandra* data from Xue et al. (2011) utilized in Mullaney et al. (2015). The rest-frame 2–8 keV luminosities of the field and protocluster AGNs are $L_{2-8\,\mathrm{keV}} \approx 10^{42}$–$2 \times 10^{44}$ erg s^{-1} and $L_{2-8\,\mathrm{keV}} \approx 4 \times 10^{43}$–$2 \times 10^{44}$ erg s^{-1}, respectively; we have converted the X-ray luminosities of the field and protocluster AGNs to a common rest-frame 2–8 keV luminosity assuming a typical X-ray spectral slope of $\Gamma = 1.9$ (see footnote 1). However, the lack of lower luminosity AGNs in the protocluster sample should not affect our comparison since the average SFRs of AGNs are not a function of X-ray luminosity over the redshift and luminosity ranges of our sources, at least for field AGNs (e.g. Mullaney et al. 2012; Rosario et al. 2012; Stanley et al. 2015). Since the SFR is broadly proportional to the galaxy mass in star-forming galaxies (i.e. what is often referred to as the 'main sequence'; e.g. Elbaz et al. 2011; Speagle et al. 2014; Schreiber et al. 2015), it is also useful to consider the stellar masses of the AGN host galaxies. The stellar masses of the field AGNs in Mullaney et al. (2015) have been calculated by Santini et al. (2012) from fitting AGN and host-galaxy templates to the rest-frame optical–near-IR data. The stellar masses cover (0.2–3) $\times 10^{11}$ M$_\odot$ and the mean stellar mass is $\approx 5 \times 10^{10}$ M$_\odot$, which corresponds to M_* over the redshift range of the field AGNs (e.g. Ilbert et al. 2013). The stellar masses of the protocluster AGNs have been calculated by Kubo et al. (2015) from fitting host-galaxy templates to the rest-frame optical–near-IR data. Excluding the three protocluster AGNs with broad optical emission lines (AGN 1; AGN 4; AGN 7; Steidel et al. 2003; Yamada et al. 2012b; Kubo et al. 2015), which indicate the presence of an unobscured AGN at optical wavelengths that will contaminate the host-galaxy mass measurements, the range in stellar masses is (0.3–2) $\times 10^{11}$ M$_\odot$, with a mean of $\approx 6 \times 10^{10}$ M$_\odot$. On the basis of this stellar mass comparison, there are no significant differences between the field and protocluster AGNs, although we note that the protocluster AGN sample is small and that there are significant uncertainties on the stellar masses of individual sources.

In Fig. 3, we plot the infrared luminosity from star formation versus redshift for the X-ray AGNs in the protocluster and the field. Using equation (1) to convert from L_{IR} to SFR, the SFRs of the three ALMA-detected X-ray AGNs are $\approx$220–410 M$_\odot$ yr^{-1} and the SFR upper limits for the five ALMA-undetected X-ray AGNs are $\lesssim$210 M$_\odot$ yr^{-1} (the SFR upper limits range from $<$130 M$_\odot$ yr^{-1} to $<$210 M$_\odot$ yr^{-1}). These SFRs are broadly similar to those calculated for the X-ray AGNs in the field, although to make a more quantitative comparison we need to calculate mean SFRs. Many of the X-ray AGNs in the protocluster and field have SFR upper limits, precluding the calculation of a mean, and we have therefore adopted a simple approach to calculate the range in mean SFR that covers all possibilities. The lower limit on the mean SFR is calculated assuming that the SFRs of the sources with SFR upper limits have the extreme value of 0 M$_\odot$ yr^{-1} while an upper limit

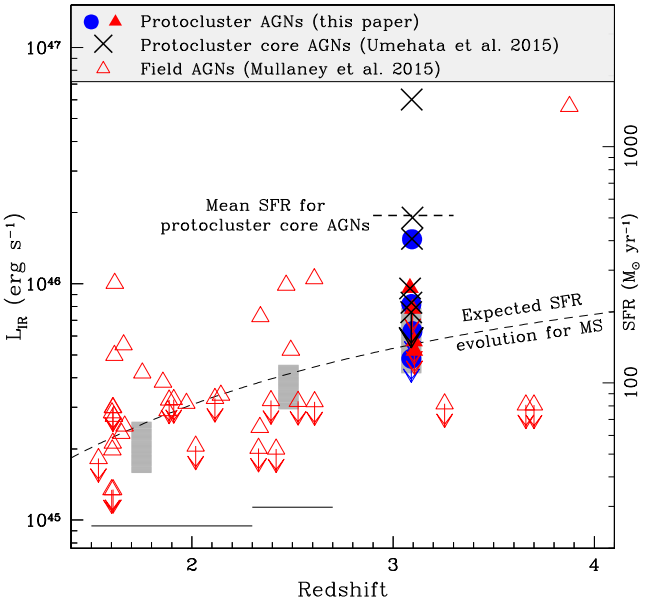

Figure 3. Infrared luminosity from star formation versus redshift for the X-ray detected AGNs in the SSA 22 protocluster from this paper compared to X-ray detected AGNs in the protocluster core (crosses; taken from Umehata et al. 2015) and X-ray-detected AGNs in the field (open triangles; taken from Mullaney et al. 2015); see Fig. 1 for the other symbol descriptions. The conversion from L_{IR} to SFR is calculated using equation (1). The shaded regions indicate the range in mean infrared luminosities for the protocluster AGNs at $z \approx 3.09$ (excluding the Umehata et al. 2015 data) and for the AGNs in the field at two mean redshifts; the redshift ranges are indicated by the black horizontal lines. The widths of the shaded regions are arbitrary. The dashed line indicates the mean infrared luminosity for the protocluster AGNs at the core (using the Umehata et al. 2015 data) and the dashed curve indicates the measured evolution in infrared luminosity for an M_* star-forming galaxy over $z = 1.4$–4.1 from Schreiber et al. (2015), using the definition of M_* from Ilbert et al. (2013). There is significant scatter in the infrared luminosities for individual X-ray AGNs; however, the mean infrared luminosities are consistent with M_* star-forming galaxies at the average redshifts for both the protocluster AGN from this paper and the field AGN samples. Including the Umehata et al. (2015) data shows that the infrared luminosities are significantly enhanced for the AGNs at the protocluster core.

is calculated by assuming that the SFRs are set at the upper limit values. This approach is conservative since the true mean SFR for each of the samples must lie within the calculated ranges. Using this approach, we calculated the following ranges in mean SFR: 110–210 M$_\odot$ yr^{-1} for the protocluster AGNs, 80–120 M$_\odot$ yr^{-1} for the $z = 2.3$–2.7 field AGNs (mean $z = 2.48$), and 40–70 M$_\odot$ yr^{-1} for the $z = 1.5$–2.3 field AGNs (mean $z = 1.75$). A simple comparison of these ranges in mean SFR shows that the protocluster AGNs have elevated SFRs over AGNs in the field. However, to provide a more accurate comparison we must also take into account the expected evolution in SFR with redshift of the field AGNs out to the higher redshift of the protocluster.

The SFRs of X-ray AGNs in the field are found to track the evolution of massive star-forming galaxies (galaxies with masses around M_*, the knee of the stellar-mass function; e.g. Mullaney et al. 2012; Santini et al. 2012; Hickox et al. 2014; Stanley et al. 2015) and therefore when accounting for the expected evolution in SFR with redshift of the field AGNs we have assumed the measured SFR evolution for M_* star-forming galaxies from Schreiber et al. (2015); we recall that the mean stellar mass of the protocluster AGNs is

also consistent with M_*. On the basis of this approach, we expect a factor ≈2.2 enhancement in mean SFR from $z = 1.75$ to $z = 3.09$ (giving a predicted range of 90–150 $M_\odot$ yr^{-1} for the field AGNs at $z = 3.09$) and a factor ≈1.3 enhancement in mean SFR from $z = 2.48$ to $z = 3.09$ (giving a predicted range of 100–160 $M_\odot$ yr^{-1} for the field AGNs at $z = 3.09$). Taking account of this assumed global evolution in SFR, the mean ranges in SFR between the X-ray AGNs in the field and protocluster are now broadly consistent; see Fig. 3. Assuming the lowest and highest values in the mean SFR ranges for the field and protocluster AGNs, the mean SFRs of the protocluster AGNs are enhanced by a factor of ≈0.7–2.3 over the mean SFRs of the field AGNs.

Overall our results indicate that the growth rates of individual AGN host galaxies in a protocluster environment are not significantly elevated over those of AGNs in the field. The masses and SFRs of both the protocluster and field AGNs are also similar to those of typical massive (M_*) star-forming galaxies; see Fig. 3. However, consideration of the spatial location of the ALMA-detected AGNs in the protocluster indicates that there may be an environmental dependence on the mean SFRs. The three ALMA-detected AGNs in our sample (AGN 1; AGN 5; AGN 8) lie within the core of the protocluster, at the intersection of three filamentary structures traced by LAEs (Matsuda et al. 2005; see fig. 3 of Umehata et al. 2015). Umehata et al. (2015) mapped this central region over 1.5 arcmin × 3.0 arcmin (≈0.7 × 1.4 Mpc) with ALMA at 1.1 mm and measured a ≈2 orders of magnitude increase in the SFR density in this region of the protocluster when compared to the field. It is therefore potentially significant that the three ALMA-detected AGNs in our sample lie within this high-SFR region. These ALMA-detected AGNs were also detected at 1.1 mm by Umehata et al. (2015), in addition to another two X-ray AGNs spectroscopically identified to lie in the protocluster (a third X-ray AGN with a photometric redshift consistent with the protocluster redshift was undetected at 1.1 mm). How much does the mean SFR change if we include these three additional X-ray AGNs that lie in the protocluster core? Allowing for the 0.1 dex increase in $L_{\rm IR}$ between the star-forming galaxy templates adopted in our study and those adopted in Umehata et al. (2015), the range in mean SFR for the 11 X-ray AGNs is 270–360 $M_\odot$ yr^{-1}, leading to a factor of ≈1.7–4.0 enhancement in mean SFR over that measured in the field. However, we note that the majority of the increase in mean SFR is driven by a single extreme object which has a SFR that is $\gtrsim$3 times larger than any of the other X-ray AGNs (ADF 22a in Umehata et al. 2015 with an implied SFR of 1600 $M_\odot$ yr^{-1} for the templates adopted in our study). ADF 22a is the brightest submillimetre galaxy in the SSA 22 protocluster (Umehata et al. 2014) and appears to lie at the bottom of the protocluster gravitational potential and may be the progenitor of the brightest cluster galaxy (e.g. Tamura et al. 2010; Umehata et al. 2015).

These results indicate that, while there is a lack of significant enhancement in SFR for the protocluster AGNs in our initial sample, the star formation in the highest density region within the core of the protocluster is significantly enhanced. For example, the range in mean SFR for just the six X-ray AGNs in the protocluster core mapped by Umehata et al. (2015) is 500–530 $M_\odot$ yr^{-1}, a factor of ≈3.1–5.9 enhancement in mean SFR over that measured in the field. However, these measurements are significantly elevated by ADF 22a; removing ADF 22a from the sample gives a range in mean SFR of 280–320 $M_\odot$ yr^{-1} and a factor of ≈1.8–3.6 enhancement in SFR over the field. We also note that Lehmer et al. (2009a) found evidence that the enhancement in the fraction of galaxies hosting AGN activity found by Lehmer et al. (2009b) is highest in the densest regions of the protocluster, indicating an increase in the duty cycle of AGN activity which may be connected to the elevated star formation found here. To provide a more accurate assessment of the star formation in the protocluster and its connection to AGN activity would require sensitive SFR measurements for all of the AGNs and the galaxies across the extent of the protocluster, which would also allow for detailed BH–galaxy growth comparisons as a function of local galaxy density (e.g. Lehmer et al. 2009b, 2013; Umehata et al. 2015).

3.2 Star formation associated with Lyman-alpha blobs

Four of the X-ray AGNs studied here are hosted within LABs (LAB 2; LAB 3; LAB 12; LAB 14), which provides the opportunity to investigate the star formation properties for a subset of the LAB population. The origin of the extended Lyα emission from LABs is a matter of significant debate (e.g. Fardal et al. 2001; Geach et al. 2005, 2009; Nilsson et al. 2006; Dijkstra & Loeb 2009; Faucher-Giguère et al. 2010; Cen & Zheng 2013; Overzier et al. 2013; Ao et al. 2015; Prescott et al. 2015), with three leading possibilities: (1) the cooling of pristine gas within the dark-matter halo, potentially fed by so-called cold-gas streams, (2) the heating of gas by AGN activity (photoionization or AGN-driven jets), and (3) the heating of gas by star formation processes (photoionization by young stars or supernovae-driven winds). Previous studies of the LABs in the SSA 22 protocluster have suggested that the extended Lyα emission is predominantly due to the heating of the gas rather than cooling (e.g. Bower et al. 2004; Geach et al. 2005, 2009, 2014; Wilman et al. 2005; Smith et al. 2008; Webb et al. 2009; Colbert et al. 2011; Hayes, Scarlata & Siana 2011). By selection, all of our ALMA-observed LABs host X-ray AGNs which, as shown by Geach et al. (2009), already provides a potential source of heating for the Lyα emission through photoionization. However, all of the four LABs also host an ALMA source, either directly associated with the X-ray AGN or within the extent of the Lyα emission, which indicates the presence of luminous star formation; see Tables 1 and 2.

Using equation (1) to convert from $L_{\rm IR}$ to SFR, the range of SFRs for the LABs is found to be ≈150–410 $M_\odot$ yr^{-1} and the mean and standard deviation is 240 ± 110 $M_\odot$ yr^{-1}. The range and mean of the SFRs are consistent with those found for massive star-forming galaxies at $z \approx 3$ (≈150 $M_\odot$ yr^{-1} for M_*; e.g. Schreiber et al. 2015) and, therefore, the X-ray-detected LABs do not appear to have significantly elevated SFRs when compared to the field; see Fig. 3. This mean SFR is also comparable to that implied from the mean submillimetre flux found by stacking the low-resolution single-dish submillimetre data of the most extended LABs in the SSA 22 protocluster (LABs 1–12; ≈190 ± 40 $M_\odot$ yr^{-1}; Hine et al. 2016b), which are similar systems to the LABs explored here. By comparison the mean SFR for all of the LABs in the SSA 22 protocluster is $\gtrsim$2 times lower than that calculated here but includes many more compact systems (≈80 ± 30 $M_\odot$ yr^{-1}; Hine et al. 2016b). Interestingly, the two giant LABs in our sample (LAB 2; LAB 3), with physical extents of $\gtrsim$100 kpc (Matsuda et al. 2011), do not host more luminous star formation than the two smaller ALMA-detected LABs despite being an order of magnitude more luminous in Lyα emission. To first order, this suggests that star formation activity has less of an effect on the production of the extended Lyα emission in the giant LABs than for the smaller LABs.

We can quantify the potential contribution to the Lyα emission from photoionization in LABs by taking the same approach as Geach et al. (2009) and calculate the ratio between the 200–912 Å

luminosity from star formation (i.e. the ultraviolet wavelengths where the photon energies are high enough to produce Lyα through photoionization) and the Lyα luminosity. In this calculation, we take our infrared-derived star formation luminosities and convert them to 200–912 Å luminosities assuming the star-forming galaxy template adopted in Geach et al. (2009), which provides a good characterization of the composite SED of the X-ray-detected LABs in the SSA 22 protocluster. On the basis of this approach we find that the luminosity at 200–912 Å due to star formation is always at least an order of magnitude higher than the Lyα luminosity and can be responsible for producing the Lyα luminosity with the following escape fractions of 200–912 Å photons: ≈5 per cent (LAB 2), ≈3 per cent (LAB 3), ≈0.3 per cent (LAB 12), and ≈0.2 per cent (LAB 14). By comparison, the average escape fraction for all of the LABs in the protocluster is ≈2 per cent, based on the mean SFR from Hine et al. (2016b) and the mean Lyα luminosity for the LABs. The infrared luminosities of the LABs indicate that they harbour dust-obscured star formation and we would therefore expect only a small fraction of the 200–912 Å photons to be able to directly escape and photoionize the extended Lyα emission. Geach et al. (2009) estimated that the average escape fraction for LABs is ≈0.6 per cent; however, we note that, given the factor ≈5 decrease in the stacked submillimetre flux for the LABs in the SSA 22 protocluster between the Geach et al. (2009) study and Hine et al. (2016b), an average escape fraction of ≈3 per cent is more plausible. We also note that this is effectively a lower limit on the average escape fraction since it assumes that the ultraviolet emission is only due to star formation, when there is likely to also be a contribution from AGN activity. Indeed, more accurate assessments of the escape fraction based on high spatial resolution ALMA and *HST*-Space Telescope Imaging Spectrograph observations indicate that the escape fraction varies substantially across individual sources (likely due to the patchiness of the obscured dust) but can reach values in excess of ≈10 per cent (J. E. Geach, in preparation). Despite these caveats we note that our calculated escape fractions are broadly consistent with those estimated for star-forming galaxies at $z \approx 3$ (e.g. Iwata et al. 2009; Siana et al. 2015).

Therefore, on the basis of our results, star formation appears to be a plausible mechanism to produce the Lyα emission for all of the LABs explored here, although the escape fraction of 200–912 Å photons for LAB 2 and LAB 3 need to be comparatively high. As calculated by Geach et al. (2009), AGN activity also appears to be sufficient to be able to produce the Lyα luminosity for all of the X-ray-detected LABs in our sample (e.g. on the basis of the Lyα/X-ray luminosity ratio; see fig. 4 in Geach et al. 2009). However, since the ALMA sources for LAB 2 and LAB 3 are offset from the centre of the Lyα emission and the X-ray AGN, it is also possible that multiple systems photoionize the Lyα emission in these giant LABs (as also potentially found for LAB 1; Weijmans et al. 2010) and deeper ALMA observations may reveal fainter star-forming galaxy components. We finally note that, since the ALMA sources are unresolved in these four LABs (see Section 2.3), this places $\lesssim$11 kpc constraints on the physical scale of the star formation emission region.

4 CONCLUSIONS

We have presented ALMA 870 μm observations and calculated the SFRs of eight X-ray-detected AGNs, four of which reside within LABs, in the $z \approx 3.1$ SSA 22 protocluster. With these data we have found the results as follows.

(i) Three of the protocluster AGNs are detected by ALMA and have implied SFRs of ≈220–410 $M_\odot$ yr^{-1}; the non-detection of the other AGNs places SFR upper limits of $\lesssim$210 $M_\odot$ yr^{-1}. The mean SFR of the protocluster AGNs (≈110–210 $M_\odot$ yr^{-1}) is consistent (within a factor of ≈0.7–2.3) with that found for co-eval AGNs in the field, implying that galaxy growth is not significantly accelerated across the protocluster environment. However, when also considering ALMA data from the literature, we find some evidence for significantly elevated mean SFRs (up to a factor of ≈5.9 over the field) for the AGNs at the core of the protocluster, indicating that the mean growth of galaxies is accelerated in the central region. We note that the mean SFR at the protocluster core is significantly enhanced by a single extreme object, potentially the progenitor of the brightest cluster galaxy, with a SFR of ≈1600 $M_\odot$ yr^{-1}.

(ii) All four of the protocluster LABs are associated with an ALMA source within the extent of their Lyα emission, indicating the presence of vigorous star formation. The ALMA sources in the two giant LABs in our sample are offset from the X-ray AGNs but are likely to be physically associated with the LABs. The SFRs of the LABs are comparatively modest (≈150–410 $M_\odot$) and are consistent with those expected for co-eval massive star-forming galaxies. Furthermore, the giant LABs do not host more luminous star formation than the smaller LABs, despite being an order of magnitude more luminous in Lyα emission.

(iii) On the basis of the star formation and Lyα luminosity of the LABs, we conclude that star formation can power the extended Lyα emission (through photoionization) for all of the LABs explored here, although the escape fraction of 200–912 Å photons will need to be relatively high for the two giant LABs (LAB 2 and LAB 3). However, since the ALMA sources in the giant LABs are offset from the centre of the Lyα emission and the X-ray AGN, it is also possible that multiple systems photoionize the Lyα emission and deeper ALMA observations may reveal fainter star-forming galaxy components.

Overall, our study has provided a mixed message on the mean SFRs of X-ray AGNs in a protocluster environment. From our original ALMA sample, which explored a range of regions across the protocluster, there was no strong evidence for a significant enhancement in mean SFR for the protocluster AGNs over that found for AGNs in the field. However, when including ALMA data for AGNs in the protocluster core from Umehata et al. (2015), evidence was found for elevated mean SFRs over the field, although the mean SFR was dominated by one exceptional protocluster AGN with a SFR $\gtrsim$3 times higher than the other AGNs. Our results therefore provide evidence that star formation is enhanced for the AGNs in the central region of the protocluster but is consistent with field AGNs outside of this central region. To more comprehensively measure how much the protocluster environment affects star formation would require a complete census of star formation across the whole of the protocluster for both AGNs *and* galaxies. Mapping the protocluster with ALMA would achieve this aim and, when combined with the deep *Chandra* observations, would also allow for detailed BH–galaxy growth comparisons across the full protocluster environment.

ACKNOWLEDGEMENTS

We thank the referee for a constructive and useful review of the paper. We gratefully acknowledge support from the Leverhulme Trust (DMA), the Science and Technology Facilities Council (DMA; CMH; IRS; DJR; AMS; ST/L00075X/1), the ERC Advanced Investigator grant DUSTYGAL 321334 (JMS; IRS), a Royal Society

Wolfson Merit Award (IRS), the Collaborative Research Council 956, subproject A1, funded by the Deutsche Forschungsgemeinschaft (AK), KAKENHI (YM; 20647268), the Durham Doctoral Scholarship (FS), and the Grant-in-Aid for JSPS Fellows (HU; 26.11481). This paper makes use of the following ALMA data: ADS/JAO.ALMA#2011.0.00725.S. ALMA is a partnership of ESO (representing its member states), NSF (USA), and NINS (Japan), together with NRC (Canada) and NSC and ASIAA (Taiwan), in cooperation with the Republic of Chile. The Joint ALMA Observatory is operated by ESO, AUI/NRAO, and NAOJ.

REFERENCES

Alexander D. M., Hickox R. C., 2012, New Astron. Rev., 56, 93
Alexander D. M. et al., 2008, ApJ, 687, 835
Ao Y. et al., 2015, A&A, 581, A132
Benson A. J., 2010, Phys. Rep., 495, 33
Béthermin M. et al., 2015, A&A, 573, A113
Bower R. G. et al., 2004, MNRAS, 351, 63
Brandl B. R. et al., 2006, ApJ, 653, 1129
Brandt W. N., Alexander D. M., 2015, A&AR, 23, 1
Capak P. L., Teplitz H. I., Brooke T. Y., Laher R., Science Center S., 2013, American Astronomical Society Meeting Abstracts #221, 221, #340.06
Cen R., Zheng Z., 2013, ApJ, 775, 112
Chabrier G., 2003, PASP, 115, 763
Chiang Y.-K., Overzier R., Gebhardt K., 2013, ApJ, 779, 127
Colbert J. W., Scarlata C., Teplitz H., Francis P., Palunas P., Williger G. M., Woodgate B., 2011, ApJ, 728, 59
De Lucia G., Springel V., White S. D. M., Croton D., Kauffmann G., 2006, MNRAS, 366, 499
Del Moro A. et al., 2016, MNRAS, 456, 2105
Dijkstra M., Loeb A., 2009, MNRAS, 400, 1109
Draine B. T., Li A., 2007, ApJ, 657, 810
Elbaz D. et al., 2011, A&A, 533, A119
Fardal M. A., Katz N., Gardner J. P., Hernquist L., Weinberg D. H., Davé R., 2001, ApJ, 562, 605
Faucher-Giguère C.-A., Kereš D., Dijkstra M., Hernquist L., Zaldarriaga M., 2010, ApJ, 725, 633
Geach J. E. et al., 2005, MNRAS, 363, 1398
Geach J. E. et al., 2009, ApJ, 700, 1
Geach J. E. et al., 2014, ApJ, 793, 22
Governato F., Baugh C. M., Frenk C. S., Cole S., Lacey C. G., Quinn T., Stadel J., 1998, Nature, 392, 359
Graham A. W., Scott N., 2013, ApJ, 764, 151
Harrison C. M. et al., 2012, ApJ, 760, L15
Hayashino T. et al., 2004, AJ, 128, 2073
Hayes M., Scarlata C., Siana B., 2011, Nature, 476, 304
Hickox R. C., Mullaney J. R., Alexander D. M., Chen C.-T. J., Civano F. M., Goulding A. D., Hainline K. N., 2014, ApJ, 782, 9
Hine N. K., Geach J. E., Alexander D. M., Lehmer B. D., Chapman S. C., Matsuda Y., 2016a, MNRAS, 455, 2363
Hine N. K. et al., 2016b, MNRAS, 460, 4075
Hodge J. A. et al., 2013, ApJ, 768, 91
Ilbert O. et al., 2013, A&A, 556, A55
Iwata I. et al., 2009, ApJ, 692, 1287
Kauffmann G., Nusser A., Steinmetz M., 1997, MNRAS, 286, 795
Kennicutt R. C., Jr, 1998, ARA&A, 36, 189
Kormendy J., Ho L. C., 2013, ARA&A, 51, 511
Kubo M. et al., 2013, ApJ, 778, 170
Kubo M., Yamada T., Ichikawa T., Kajisawa M., Matsuda Y., Tanaka I., 2015, ApJ, 799, 38
Lehmer B. D. et al., 2009a, MNRAS, 400, 299
Lehmer B. D. et al., 2009b, ApJ, 691, 687
Lehmer B. D. et al., 2013, ApJ, 765, 87
McMullin J. P., Waters B., Schiebel D., Young W., Golap K., 2007, in Shaw R. A., Hill F., Bell D. J., eds, ASP Conf. Ser. Vol. 376, Astronomical Data Analysis Software and Systems XVI. Astron SOc. Pac., San Francisco, p. 127
Matsuda Y. et al., 2004, AJ, 128, 569
Matsuda Y. et al., 2005, ApJ, 634, L125
Matsuda Y. et al., 2011, MNRAS, 410, L13
Mullaney J. R., Alexander D. M., Goulding A. D., Hickox R. C., 2011, MNRAS, 414, 1082
Mullaney J. R. et al., 2012, MNRAS, 419, 95
Mullaney J. R. et al., 2015, MNRAS, 453, L83
Netzer H. et al., 2007, ApJ, 666, 806
Nilsson K. K., Fynbo J. P. U., Møller P., Sommer-Larsen J., Ledoux C., 2006, A&A, 452, L23
Overzier R. A., Nesvadba N. P. H., Dijkstra M., Hatch N. A., Lehnert M. D., Villar-Martín M., Wilman R. J., Zirm A. W., 2013, ApJ, 771, 89
Prescott M. K. M., Momcheva I., Brammer G. B., Fynbo J. P. U., Møller P., 2015, ApJ, 802, 32
Richards G. T. et al., 2006, ApJS, 166, 470
Rosario D. J. et al., 2012, A&A, 545, A45
Rosario D. J. et al., 2013, ApJ, 771, 63
Saez C. et al., 2015, MNRAS, 450, 2615
Santini P. et al., 2012, A&A, 540, A109
Schreiber C. et al., 2015, A&A, 575, A74
Scott S. E., Dunlop J. S., Serjeant S., 2006, MNRAS, 370, 1057
Shao L. et al., 2010, A&A, 518, L26
Siana B. et al., 2015, ApJ, 804, 17
Simpson J. M. et al., 2015, ApJ, 807, 128
Smith D. J. B., Jarvis M. J., Lacy M., Martínez-Sansigre A., 2008, MNRAS, 389, 799
Speagle J. S., Steinhardt C. L., Capak P. L., Silverman J. D., 2014, ApJS, 214, 15
Stanley F., Harrison C. M., Alexander D. M., Swinbank A. M., Aird J. A., Del Moro A., Hickox R. C., Mullaney J. R., 2015, MNRAS, 453, 591
Steidel C. C., Adelberger K. L., Dickinson M., Giavalisco M., Pettini M., Kellogg M., 1998, ApJ, 492, 428
Steidel C. C., Adelberger K. L., Shapley A. E., Pettini M., Dickinson M., Giavalisco M., 2000, ApJ, 532, 170
Steidel C. C., Adelberger K. L., Shapley A. E., Pettini M., Dickinson M., Giavalisco M., 2003, ApJ, 592, 728
Tamura Y. et al., 2009, Nature, 459, 61
Tamura Y. et al., 2010, ApJ, 724, 1270
Tamura Y. et al., 2013, MNRAS, 430, 2768
Umehata H. et al., 2014, MNRAS, 440, 3462
Umehata H. et al., 2015, ApJ, 815, L8
Webb T. M. A., Yamada T., Huang J.-S., Ashby M. L. N., Matsuda Y., Egami E., Gonzalez M., Hayashimo T., 2009, ApJ, 692, 1561
Weijmans A.-M., Bower R. G., Geach J. E., Swinbank A. M., Wilman R. J., de Zeeuw P. T., Morris S. L., 2010, MNRAS, 402, 2245
Wilman R. J., Gerssen J., Bower R. G., Morris S. L., Bacon R., de Zeeuw P. T., Davies R. L., 2005, Nature, 436, 227
Xue Y. Q. et al., 2011, ApJS, 195, 10
Yamada T., Nakamura Y., Matsuda Y., Hayashino T., Yamauchi R., Morimoto N., Kousai K., Umemura M., 2012a, AJ, 143, 79
Yamada T., Matsuda Y., Kousai K., Hayashino T., Morimoto N., Umemura M., 2012b, ApJ, 751, 29

This paper has been typeset from a TEX/LATEX file prepared by the author.